Characterization of the isolated $[Co_3Ni(EtOH)]^+$ cluster by IR spectroscopy and spin-dynamics calculations

D. Dutta,[1] M. Becherer,[2] D. Bellaire,[2] F. Dietrich,[2] M. Gerhards,[2] G. Lefkidis,[1,*] and W. Hübner[1]

[1]*Department of Physics and Research Center OPTIMAS, Technische Universität Kaiserslautern, PO Box 3049, 67653 Kaiserslautern, Germany*

[2]*Department of Chemistry and Research Center OPTIMAS, Technische Universität Kaiserslautern, Erwin-Schrödinger-Straße 52, Germany*

(Received 23 December 2017; revised manuscript received 30 April 2018; published 5 June 2018)

We experimentally and theoretically study the geometry, as well as the electronic and vibrational properties, of the heterotetranuclear magnetic cluster $[Co_3Ni(EtOH)]^+$, which is prepared in the gas phase with molecular beam expansion. We characterize the cluster and identify possible isomers through the comparison of experimentally observed infrared spectra with state-of-the-art quantum chemistry calculations, more specifically by focusing on the OH stretching frequency. Furthermore, we suggest ultrafast, laser-induced, local spin-flip scenarios on every Co atom, and report a cooperative effect, in which the spin density is localized on one Co atom, gets transiently transferred to another, and then bounces back pointing in the opposite direction. Finally, we predict a tolerance of the suggested scenarios with respect to the laser detuning of about 20 meV, which lies within an experimentally applicable range. Our joint investigation is an additional step toward the implementation of laser-controlled nanospintronic devices.

DOI: 10.1103/PhysRevB.97.224404

I. INTRODUCTION

After the discovery of laser-induced demagnetization by Beaurepaire *et al.* in 1996 [1], there has been a huge amount of theoretical and experimental progress in the field of femtomagnetism [2,3]. In the subfield of transition-metal nanomagnets, extensive experimental and theoretical work has been done on small nickel and cobalt clusters [4,5]. Additionally, several studies of subpicosecond laser-induced spin dynamics on similar clusters have already been performed [6,7].

With respect to the experimental investigations of isolated metal clusters with different ligands by using an ablation source [8,9] in combination with the Infrared Multiphoton Dissociation (IRMPD) technique (cf., e.g., Refs. [10,11]), a variety of investigations have been performed (cf., e.g., Refs. [12–21]; Refs. [12,16–18,20] specifically refer to aggregates with alcohol molecules). The infrared (IR) spectra in combination with density functional theory (DFT) and quantum chemistry calculations yield structural assignments of the isolated transition metal/ligand clusters.

From a chemical point of view, many material characteristics can be understood at a molecular level through the investigation of clusters. By revealing the behavior of the smallest possible atomic constructs, a better understanding of macroscopic effects and properties can be achieved.

Both Ni and Co are known for their catalytic activity as well as their magnetic behavior, two aspects of high interest regarding materials science. As an example, it has been shown that a mix of the two metals in a catalyst compound increases its performance for the methane reforming process through the suppression of deactivation mechanisms (e.g., carbon formation or catalyst oxidation) [22]. Numerous studies on the activation of small molecules for cobalt as well as nickel have been published (e.g., H_2 [23], H_2O [13,24], and methanol [16]).

The goal of the present paper is to further elucidate the microscopic mechanisms behind an elementary laser-induced spin-manipulation process, namely the spin flip, which is crucial in nanospintronic devices. We investigate the process in a real, synthesized molecule. The reason is twofold: to have the possibility to assert the quality of our quantum-chemical calculations through comparison to experiment, and thus to make sure that our scenarios are realistic, as well as to further increase the pool of synthesizable structures, which are suitable candidates for magnetic-logic building blocks.

Here, we present the investigation of a cationic cluster consisting of the first row transition metals cobalt and nickel and an attached ethanol (EtOH) ligand, namely the heterotetranuclear cluster $[Co_3Ni(EtOH)]^+$. This cluster, compared to analogous homotetranucelar ones such as Ni_4 [25–27] or Co_4 [28,29], has a slightly lower symmetry, which leads to stronger spin localization [30] and thus opens the way for localized spin-manipulation scenarios. Based on the knowledge at our disposal, $[Co_3Ni(EtOH)]^+$ has great possibility to act as a prototype for ultrafast spin dynamics, aiming at fast data processing. For this, the spin takes over the role of the information carrier (bit) [31]. We structurally analyze the metallic cluster and investigate its potential to function as a magnetic-logic element.

The attached EtOH molecule serves mainly to slightly lower the symmetry of the cluster. Geometry optimization of the bare $[Co_3Ni]^+$ cluster (without EtOH) yields a C_{3v} point group symmetry, which, in turn, leads to a spin-density delocalization in the energetically low electronic states. In other words, we do not find enough electronic states with spin sitting on only one

*lefkidis@physik.uni-kl.de

or two of the Co atoms, and hence it is impossible to derive logic gates (such as AND, OR, and XOR). Previous studies have shown that one can overcome this problem by lowering the structural and electronic symmetry. This is achieved by attaching a ligand to the metallic cluster [32,33]. This way, the magnetic centers can be differentiated enough to yield spin-density localization, but not too strongly to hinder cooperative magnetic behavior between the metallic atoms [20,34–36]. Our system is positively charged. This has practical reasons (a charge is needed for the mass spectrometry), but also stems from the consideration that clusters with triplet electronic states are well-suited for magnetic logic: Two unpaired electrons allow for spin- and charge-dynamics separation [20,34], while, generally, this is not the case with doublet states, in which one electron is the carrier of both spin and charge (unless the doublet state is formed, e.g., from three or five unpaired electrons, in which case, however, the states lie energetically very high). Higher multiplicities (quintets, septets, etc.), usually render the situation too complex, without necessarily bringing much benefit with respect to the envisaged logic functionalization.

The rest of the paper is organized as follows. In Sec. II the possible geometries of the cluster, as well as the theoretical methods for their quantum chemical calculation are presented. In Sec. III a detailed analysis of the theoretically computed and the experimentally measured IR spectra, as well as their comparison is presented. In Sec. IV we theoretically investigate the possibility for ultrafast, laser-induced spin dynamics on the cluster, while, in Sec. V we summarize our findings.

II. GEOMETRY OF $[Co_3Ni(EtOH)]^+$

Experimentally, the cluster is prepared in a molecular beam experiment. Although its stoichiometry is ascertained with mass spectroscopy, its exact geometry can only be determined in an indirect way. In our case, it is determined by the use of IR spectroscopy employing the IRMPD technique and evaluated by comparison with various theoretical calculations. Several stable stereoisomers and their optimized geometries are taken into account using different theoretical levels of calculations (Fig. 1).

At a preliminary stage, we perform a less expensive computation using DFT to find all possible isomeres as well as their pertinent vibrational spectra, which are then compared with the experimental results. We use the BPW91 functional, which has proven to provide adequate results for this kind of transition metal clusters [20], and the 6-311+G(d,p) [37] basis set. We perform calculations for various multiplicities and geometries, including four ones with intact and six ones with dissociated EtOH. Figure 1 gives an overview of the most stable structures within the different geometries considered.

Then, we perform a series of quantum-chemical calculations in real-space, to get accurate excited electronic states, which we need for the spin-dynamics scenarios described later on. First, a preliminary geometry optimization step at the Hartree-Fock (HF) level is performed, where we use various basis sets (such as the Sapporo family of nonrelativistic double-zeta SPK-DZC basis set [38], the Huzinaga's 21 split-valence Midi basis set [39], and the Stevens/Basch/Krauss/Jasien/Cundari valence basis set [40])

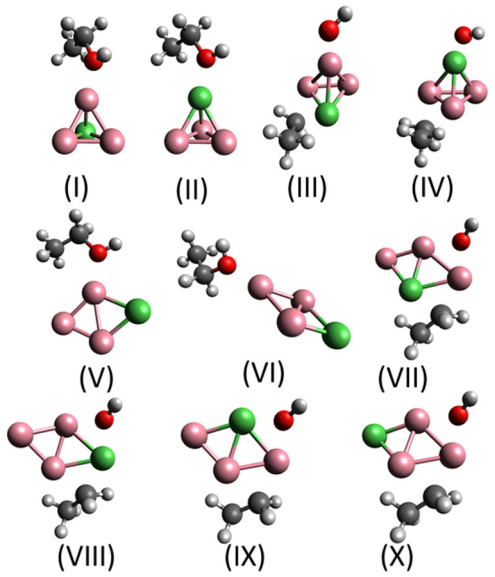

FIG. 1. All geometries considered in this study. Isomers I–V have a pyramidal metal core and V–X a rhombic metal part. Furthermore, isomers I, II, V, and VI have a nondissociated (intact) EtOH ligand attached, while in the isomers III, IV, VII, VII, IX, and X, the EtOH is dissociated in an ethyl and a hydoxyl group. Although the energetically lowest structure is isomer VII, theoretical and experimental IR spectra suggest that only nondissociated isomers are present in the experiment (see text).

and multiplicities (singlets, triplets, quintets, and septets). We consider both pyramidal and rhombic structures. Restricting ourselves only to the HF calculations wrongly predicts the latter ones as being the energetically lowest ones, if the ligand is not allowed to dissociate. As with all 3*d* transition metals, however, correlations play an extremely important role both for the electronic energies as well as for their chemical and physical properties (notably the magnetic properties). Therefore, subsequently, a series of single-point coupled-cluster calculations with single and double excitations and the perturbative inclusion of energy contributions from triple excitations [CCSD(T)] is performed. These give a very good account of the correlation energies of the *d*-block elements in our system, which is necessary to precisely predict the ground-state geometry. Finally, the excited electronic states are calculated with the equation-of-motion coupled-cluster method with single and double excitations (EOM-CCSD) on top of the CCSD-optimized structure (see Table I).

For the CCSD and the EOM-CCSD calculations, we choose sophisticated basis sets for the metal atoms (but not too complex to keep the calculations manageable) as we are interested in the spin states of the metal atoms, and relatively simple basis sets for the other atoms. Specifically, we perform the CCSD calculations using the STO-6G basis set for C and H [41], the same STO-6G basis set with an additional *d* shell for O, and the DGauss A1 DFT Coulomb Fitting basis set [42] for Co and Ni (this combination is denoted as BS1).

The excited electronic states obtained with the EOM-CCSD method from a triplet reference state are not necessarily eigenstates of the $\hat{S}^2$ operator. Since we need pure-spin excited states, we perform the EOM-CCSD calculations not starting

TABLE I. Comparison of ground-state energy for different geometries and different *ab initio* level calculations. Values are relative energies of different isomers within the same calculation method. Independent geometry optimization is performed for the HF, DFT, and EOM-CCSD level. CCSD and CCSD(T) calculations are performed using the DFT-level optimized structures. Multiplicities are given in parenthesis for the spin-adapted level of calculations. The CCSD and the CCSD(T) energies are computed with unrestricted Hartree-Fock (UHF) and therefore yield spin-contaminated states (fractional multiplicities), just like the DFT results. The EOM-CCSD calculation is based on a different closed-shell CCSD step (not shown here), and therefore yields pure-spin states (integer multiplicites). The geometry of each isomer is shown in Fig. 1.

Isomer	HF (kJ/mol)	DFT (kJ/mol)	CCSD (kJ/mol)	CCSD(T) (kJ/mol)	EOM-CCSD (kJ/mol)
I	479(7)	54(7.1)	136(7.3)	117(7.3)	120(3)
II	643(3)	50(7.0)	140(7.3)	118(7.3)	126(3)
III	-	10(7.1)	197(7.7)	146(7.7)	-
IV	-	53(7.0)	223(7.5)	183(7.5)	-
V	610(3)	147(4.4)	280(4.6)	236(4.6)	236(3)
VI	0(7)	149(5.5)	232(5.8)	206(5.8)	220(3)
VII	18(7)	0(7.1)	0(7.5)	0(7.5)	0(3)[a]
VIII	-	1(7.2)	88(7.7)	71(7.7)	-
IX	-	14(7.1)	59(7.7)	58(7.7)	-
X	-	3(7.0)	90(7.4)	64(7.4)	-

[a]The geometry optimization was performed at the (closed-shell) restricted-Hartree-Fock level.

from the energetically lowest open-shell mixed-spin CCSD state (see Table I), but from a closed-shell singlet reference state. The EOM-CCSD excited states calculated in this manner are singlets and triplets. As expected, the reference singlet state turns out not to be the energetically lowest one. It is rather a triplet state that becomes the ground state, a finding which is also consistent with our simpler HF results.

With four transition-metal atoms (13 atoms in total) the quantum chemical calculations for the system are demanding even at the HF level (we reach a convergence of 10^{-6} in the density matrix). An important criterion of the convergence is also the overlap matrix of the produced molecular orbitals (MOs) (which only minimally deviates from an identity matrix, as theoretically expected). This criterion is extremely important for the subsequent calculation of the optical transition-matrix elements, since otherwise the optical selection rules would not be properly obeyed [43,44]. Not surprisingly, the calculations at the CCSD level are quite challenging and time-consuming, and sometimes only average convergence is reached (a maximum of 10^{-3} in the density matrix for the restricted open shell calculations). Isomer I is the most stable one among the geometries with nondissociated ligands and also, as discussed later, probably the most abundant one in our experiments.

All quantum chemical calculations are performed using the GAMESS [45] and the GAUSSIAN [46] software packages.

III. INFRARED ABSORPTION SPECTRA

Here, only a short outline of the apparatus is given (details can be found elsewhere, e.g., in Ref. [17]). The setup consists of a three-chambered vacuum apparatus housing an ablation source and a reflectron time-of-flight mass spectrometer. The cluster is prepared by ablating a metal alloy rod and picking up all formed species by a molecular beam (cobalt:nickel rod—80:20, pulse power of the ablation laser ∼8 mJ, with a frequency-doubled Nd:YAG laser at 532 nm). The ethanol is seeded into the carrier gas from a cooled reservoir and the final cluster is formed. The beam is then filtered and analyzed in the mass spectrometer. By irradiating the beam with an IR laser at a transition wavelength, a dissociation is achieved and registered in the mass spectrum, i.e., the corresponding mass peak's intensity decreases. Specifically, the structurally sensitive OH stretching vibration is observed and therefore the IR spectrum is recorded in the region of 3520 cm^{-1} to 3760 cm^{-1}. The chosen pulse power of the IR laser amounts to about 12 mJ.

By performing vibrational frequency calculations at the DFT level, the property of the converged structures as an energetic minimum is verified and their vibrational spectra are obtained. Anharmonicities can be taken into account by scaling the spectra with a factor of 0.9862 (for the reference system $[Co_3(EtOH)]^+$, see Ref. [20]). It has been observed that, while producing their spectra reasonably well, the relative energies of the obtained geometries are not optimally represented. Therefore, CCSD and CCSD(T) level energies for the obtained geometries are consulted. By comparing theoretical and experimental spectra as well as relative energies (see Table I), an assignment of structure and spin state for the experimentally observed species is attempted.

A. Infrared absorption spectra at the DFT level

The recorded IRMPD spectrum of the $[Co_3Ni(EtOH)]^+$ cluster is shown for comparison both in Fig. 2 and in Fig. 3. Two bands can be identified, one at 3638 cm^{-1} and one at 3663 cm^{-1}, the latter one showing almost three times the intensity of the first band. Several different structural motifs have been calculated. The following combinations are considered: The cluster core in a pyramidal form with an intact as well as a dissociated ethanol molecule (Fig. 2); the cluster core in a rhombic geometry with again both ethanol forms (Fig. 3). A first observation is that, since there are two bands detected and each isomer only possesses one vibrational transition in this region, at least two different cluster geometries are produced under these experimental conditions.

The only calculated structures showing a transition in the region of the 3663 cm^{-1} band are the ones containing a pyramidal cluster core. Of those, the clusters coordinating an intact ethanol molecule are fitting best to the spectrum. However, it cannot be distinguished if the ethanol is bound by nickel or a cobalt atom to the cluster. The band at 3638 cm^{-1} can be attributed to a rhombic metal core structure with either an intact or a dissociated ethanol molecule. The relative energies are indicative for the dissociatively chemisorbed species. The position of the nickel atom is again not distinguishable. In fact, the CCSD and CCSD(T) level calculations also confirm this assignment. Principally, all calculated energies are raised significantly relative to the lowest energy isomer VII. However, since the energies of the structures comprising a pyramidal cluster core and a dissociated ethanol molecule experience the

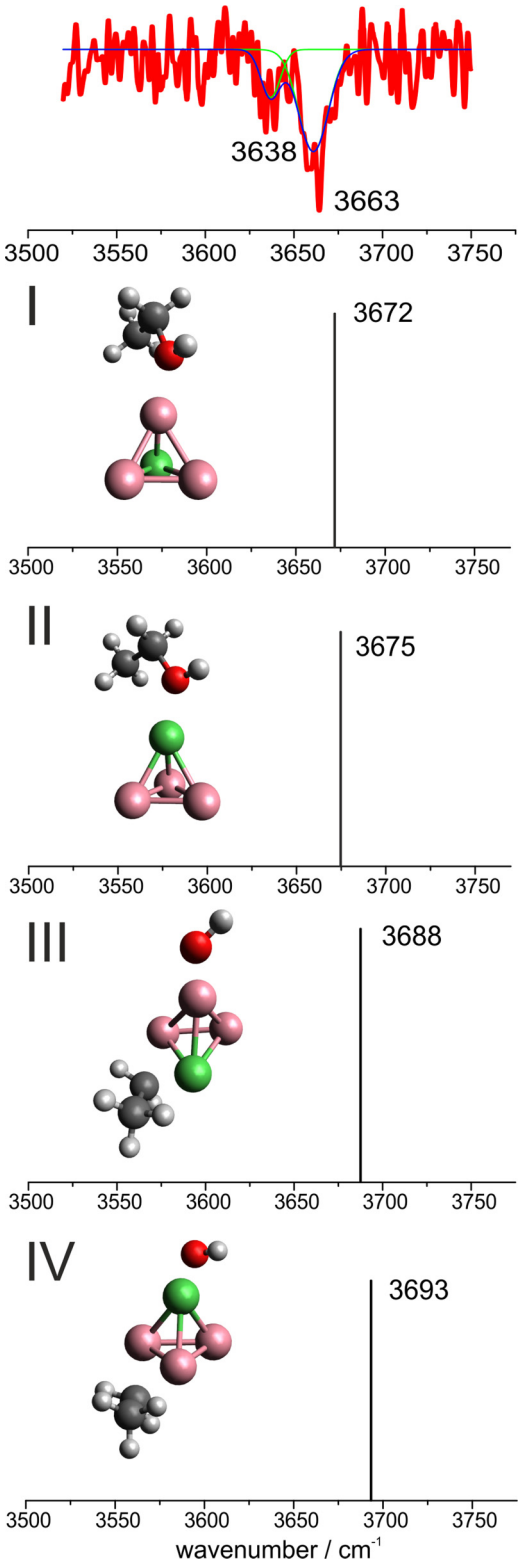

FIG. 2. Calculated pyramidal structures at the DFT level and comparison of their spectra to the measured IR spectrum.

highest raise (130 kJ/mol according to the DFT calculations), they are regarded as unlikely products. Therefore, these structures are excluded from consideration, further affirming the above assignments. A takeaway note from this investigation

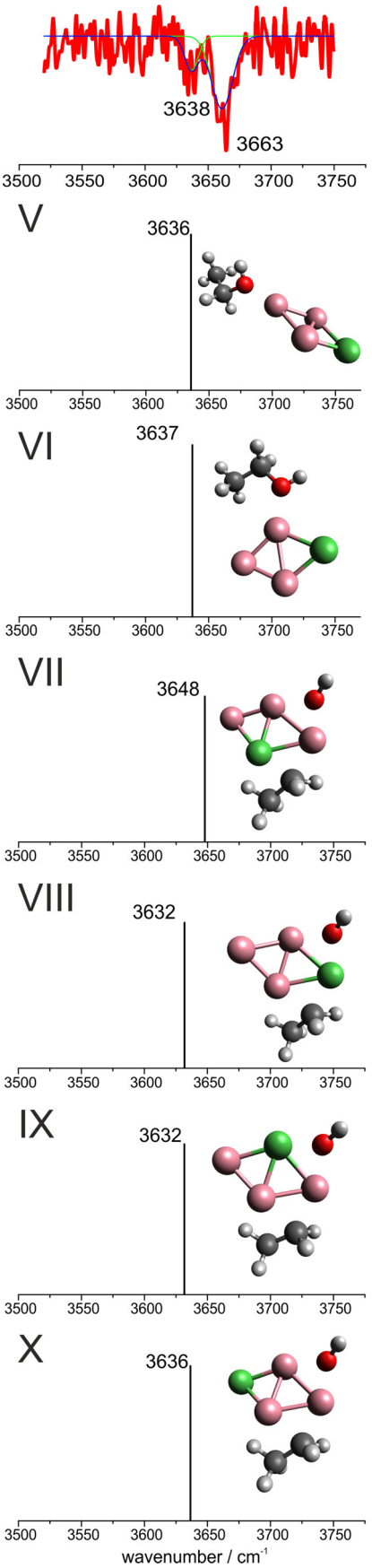

FIG. 3. Calculated rhombic structures at the DFT level and comparison of their spectra to the measured IR spectrum.

is that the OH stretching frequency depends mainly on the metal-core geometry of the cluster and not so much on whether the ligand is dissociated or not (a detailed analysis about how the metal-core geometry affects the OH stretching frequency on the CCSD level is presented later on).

At the DFT level, the different geometries considered form two groups: the more 3D-like structures (pyramidal metal core, see Fig. 2) with slightly higher OH stretching frequencies, and the more 2D-like ones (rhombic metal core, see Fig. 3) with lower OH stretching frequencies. The most probable candidate for the peak at 3663 cm^{-1} is the pyramidal isomer I attached with an intact ligand and a calculated frequency of 3672 cm^{-1} (Fig. 2). This cluster shows to be the closest to the experimentally most pronounced peak, although an overlap of isomer II with the ligand bound to the nickel cannot be excluded. The calculated OH stretching vibrations of isomer III and IV (pyramidal core geometry) reveal significant blue shifts (over 25 cm^{-1}) compared to the experimental peaks, and we therefore consider them very unlikely to have formed. Furthermore, isomers III and IV are significantly less stable than isomers I and II (cf. Table I). For further theoretical investigations, the most stable isomer I with an undissociated ethanol attached to cobalt is taken into account.

The less pronounced experimental peak at 3638 cm^{-1} is reproduced in theory with the rhombic metal core geometry (isomers V–X, see Fig. 3). It seems unlikely that isomers V and VI (with intact EtOH attached) form, since they are considerably less stable than the remaining isomers with dissociated EtOH (cf. Table I). The most stable structure is isomer VII. It is interesting to note that the shift of the OH stretching frequency at 3663 cm^{-1} between experiment and calculation observed for isomer I is similar (around 10 cm^{-1}) to the shift found for isomer VII. With respect to the relative energy and the calculated vibrational frequency from the set of the rhombic structures, isomer VII with a dissociated EtOH is most probably formed. Thus, isomer I (or II) and isomer VII can be assigned to the spectra. Nevertheless, the difference in the experimental intensities implies a higher probability of forming the intact cluster I than the dissociated structure VII, i.e., even though the metal core seems to be stabilized in the rhombic geometry when the ethanol is dissociated, with intact ethanol as well as the bare metallic cluster (without EtOH), the pyramidal geometry is favored, which can result from kinetically trapping of pyramidal metal clusters after ablation. In a further step, the alcohol moiety is attached to the metal core in the molecular beam experiment. Due to these considerations, isomer I (as most stable structure of the subset of arrangements with pyramidal metal cores) is chosen as the structure for the subsequent spin-dynamics calculations. Furthermore, in a consistent manner, the bare metallic cluster (without EtOH) also tends to the pyramidal geometry. This is another reason why we choose the pyramidal structure I for the subsequent spin-dynamics calculations.

B. Infrared absorption spectra at the CCSD level

In this section, we look at the OH stretching frequency of the structures with intact (undissociated) ligand and compare with the experiment. The ν_{OH} frequency analysis is repeated both for the HF and the CCSD reference states. At the HF level, analytical normal mode analysis is performed on geometries also obtained at the HF level (with the DGauss A1 DFT Coulomb-fitting basis set). Here ν_{OH} for closed-shell optimized structures (used as our reference state, on which our further theoretical study is done) is studied and compared with the experimental results. At the HF level, ν_{OH} for isomers I, II, V, and VI are found to be 4256 cm^{-1}, 4253 cm^{-1}, 4261 cm^{-1}, and 4264 cm^{-1}, respectively (Table II). For comparison, the value for the bare EtOH is 4076 cm^{-1}. The trend of ν_{OH} among the isomers is inconsistent with the DFT-based analysis in the previous section. However, the absolute values of ν_{OH} are systematically shifted by around 400 cm^{-1}.

TABLE II. OH stretching frequency (in cm^{-1}) of the four geometries of $[Co_3Ni(EtOH)]^+$ with undissociated EtOH at the HF (analytical values) and at the CCSD (fitted values) levels. The fitted values are calculated both in a shorter range (five converged structure data points in the region 0.961 to 1.017 Å) and a wider range (nine converged structure data points in the region 0.905 to 1.092 Å). The frequency for the CCSD values are extracted from a quadratic polynomial fit, a cubic polynomial fit but with a harmonic approximation, a cubic fit including anharmonicities beyond the harmonic approximation, and a quartic fit. All four fits are performed for geometries in which only the OH bond is varied, and also along the normal mode, as calculated analytically at the HF level. Compare also with Figs. 2 and 3 for the DFT results and the experimental data.

Isomer	Method	HF	CCSD			
			Along normal Mode		Along OH Bond	
			Wide	Short	Wide	Short
I	analytic	4256	-	-	-	-
	quadratic	-	3809	3785	3909	3796
	cubic (harmonic)	-	3943	3910	4264	3777
	cubic	-	3679	3639	3727	3421
	quartic	-	3900	3895	3986	3791
II	analytic	4253	-	-	-	-
	quadratic	-	3799	3832	3773	3799
	cubic (harmonic)	-	3950	3920	3886	3780
	cubic	-	3626	3809	3616	3799
	quartic	-	4015	3826	3795	3848
V	analytic	4261	-	-	-	-
	quadratic	-	3787	3836	3720	3780
	cubic (harmonic)	-	3914	4191	3870	3783
	cubic	-	3683	3264	3551	3677
	quartic	-	3988	4140	3832	-
VI	analytic	4264	-	-	-	-
	quadratic	-	3794	3736	3673	3782
	cubic (harmonic)	-	3931	3987	3862	3768
	cubic	-	3704	3451	3635	3690
	quartic	-	3874	3911	3880	3883

At the CCSD level, no analytical methods for the calculation of the force matrix exist and therefore numerical procedures must be used. A major challenge is that, with 13 atoms, there are altogether 33 vibrational modes (deducting three translational and three rotational modes from the altogether $3 \times 13 = 39$ degrees of freedom), which in practice translates into scanning an energy hypersurface of $3 \times 13 = 39$ dimensions (when using Cartesian coordinates for the atomic dislocations, we obviously cannot remove the translational and the rotational

motion). Furthermore, in every dimension we must collect several points to perform a decent fitting, thus rendering such an endeavor simply impossible. A simplified approach, namely to only vary the O-H distance while keeping all the other coordinates frozen, yields frequencies which are quite far from the experimental ones (both with respect to their absolute values, but more importantly also with respect to their relative values). It turns out that a more efficient way exists. First we calculate the normal modes with HF, for which analytic gradients are available [45]. Then we perform several single-point CCSD calculations along the normal-mode coordinate to extract the energy potential, and finally we fit to a polynomial function.

A fundamental question in the fitting of any curve is the number of parameters considered. Although, for our vibrational spectra, we more or less assume a harmonic potential energy profile along the vibrational mode coordinate, complete quantum chemcical calculations can also yield anharmonicities.

As the CCSD level, calculations do not reach a very tight convergence; we need to collect the energy data in a relatively wide range around the minimum to get reliable potential energy curves. Each potential curve is obtained by numerically fitting the data to a third-order polynomial. The second derivative of the potential curve at the minimum corresponds to the stretching frequency of the OH vibration. We fit to a cubic polynomial because in the relatively wide range of the sample data, the potential curve does not strictly remain within the harmonic regime. In fact, a cubic polynomial describes the classical Lennard-Jones potential around the minimum better than a quadratic one, since the latter one is symmetric (whereas the Lennard-Jones potential is steeper for shorter than the equilibrium distances, compared to the larger than the equilibrium ones). Fitting a polynomial of even higher degree does not further increase the quality of the results, despite the fact that the statistical errors for its coefficients become smaller. The reason is that we fit less than ten points, and therefore the statistical significance is not high enough. Mathematically, one could even perfectly interpolate an eighth-degree polynomial with exactly zero statistical error, which, however, would oscillate wildly in between the interpolation points.

All our frequency results are summed up in Table II. We consider two different geometry variations (along the normal mode as calculated at the HF level, and by stretching only the OH bond). We also consider two different fitting ranges (a shorter one where the O-H bond length is varied between 0.961 and 1.017 Å with five fitting points, and a wider one where the O-H bond length is varied between 0.905 and 1.092 Å with nine fitting points). Finally, we consider four different fitting methods. The first one is the simplest harmonic potential. The second one is a cubic potential (fitting a third-degree polynomial) and extracting the frequency by assuming a harmonic potential for the normal modes (strictly mathematically, the first and the second methods would yield exactly the same frequencies if the fitting points were symmetrically equidistributed around the equilibrium point at 0.987 Å, which, however, is not the case because the calculations do not converge for all chosen geometries). The third one is again the cubic potential fit but also including the cubic-term perturbations to the harmonic potential for the normal modes (anharmonicities in the phonons). Finally, the fourth one is a quartic potential fit. Figures 4 and 5 show the cubic fittings for the two pyramidal and the two rhombic geometries with undissociated ethanol attached.

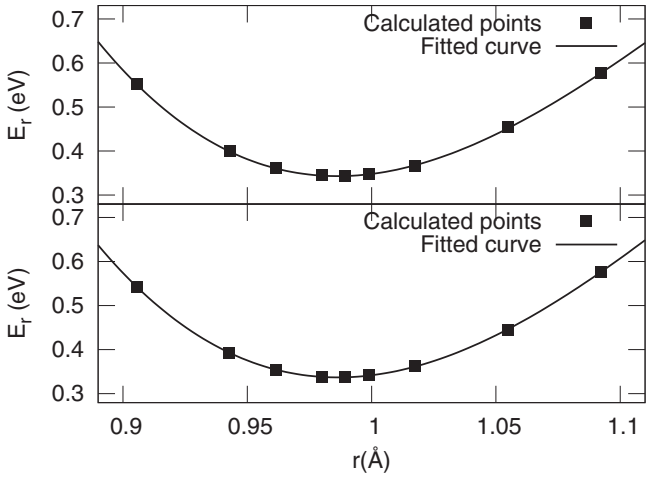

FIG. 4. Potential-energy curve fitting as a function of the O-H distance for the pyramidal structures I (lower panel) and II (upper panel), to which undissociated EtOH is attached. E_r is the relative CCSD energy and r is the O-H distance corresponding to the length of normal mode vector. Cubic polynomials are used.

Our main result, consistent with the experiment, is that the OH stretching frequency within the cubic (harmonic) approximation of our reference state of the planar isomers is red shifted with respect to the frequency of the pyramidal one (Table II). In all cases, except for quartic fittings, the trend of ν_{OH} for different isomers remains the same. The most important findings here are that correlated calculations greatly improve the frequencies (cf. HF vs. CCSD results, Table II) and that the use of a cubic potential fitting becomes better than the simple harmonic potential, however, *only* if anharmonicities are considered as well, in which case we get an excellent

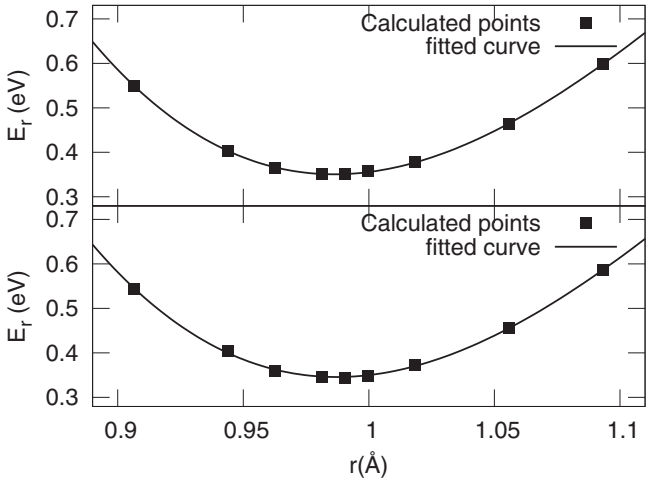

FIG. 5. Potential-energy curve fitting as a function of the O-H distance for the rhombic structures V (lower panel) and VI (upper panel), to which undissociated EtOH is attached. E_r is the relative CCSD energy and r is the O-H distance corresponding to the length of normal mode vector. Cubic polynomials are used.

TABLE III. Charge distribution of the CCSD reference state for the different isomers with undissociated EtOH ligand.

Isomer	CH_3-	-CH_2-	O	H	Co1	Co2	Co3	Ni
I	0.070	0.256	−0.265	0.330	0.099	0.285	0.281	−0.057
II	0.054	0.250	−0.246	0.318	0.289	0.324	0.317	−0.317
V	0.073	0.258	−0.272	0.331	0.053	0.181	0.191	0.186
VI	0.070	0.251	−0.265	0.327	0.082	0.229	0.232	0.073

agreement with the experimental data even at a quantitative level (e.g., for isomer I, we get $\nu_{OH} = 3679\ cm^{-1}$ as compared to the experimental peak of 3663 cm^{-1}). In general, ν_{OH} can in principle be used to distinguish between the reference states of pyramidal and planar isomers and subsequently the excited states, on which ultrafast spin-dynamics studies are performed [32].

It is clear that the OH frequency physically depends both on the geometry of the metallic part (pyramidal or rhombic), and on the species the EtOH is attached to (Co or Ni). To better understand the underlying electronic mechanisms, we also inspect the charge density of isomers I, II, V, and VI (Table III), using a gross population analysis of the reduced one-electron density matrix for the ground electronic states. It is noteworthy that in isomers I and II, the Ni is negatively charged (although in I only minimally), while the Co is always positively charged (Table III). This is in line with the fact that Ni has a higher electron affinity, almost twice that of Co [47]. Generally, a transfer of positive charge density from the metal cluster toward the ethanol ligand is observed. Since the OH is not just a simple electrostatic bond, it makes sense to look into the electronic overlap population between the O and H of the hydroxyl group. For the isomers I, II, V, and VI, the overlap densities are 0.2894, 0.2904, 0.2890, and 0.2884, respectively. Comparing the two metallic geometries, we note a slight decrease in the OH overlap population for the planar isomers. This suggests that the OH bond of the planar structures is slightly weaker, which is consistent with both the experimental and the DFT-calculated ν_{OH} values.

Finally, since we want (at least to an extent) to distinguish as much as possible between the chemical effect (i.e., whether the ligand is attached to a Co or to a Ni atom), and the geometry effect (pyramidal or rhombic), we also perform for comparison a set of CCSD calculations of two simpler, theoretically optimized structures, namely $[Co(EtOH)]^+$ and $[Ni(EtOH)]^+$ (Fig. 6).

At the HF level (where the normal modes are analytically calculated), we observe for all structures a red shift of the ν_{OH} frequency compared to the bare EtOH (consistent with the experimental results). The values for bare EtOH, $[Ni(EtOH)]^+$ and $[Co(EtOH)]^+$ are 4076 cm^{-1}, 4038 cm^{-1}, and 4041 cm^{-1}, respectively. Although the ground state of $[Co(EtOH)]^+$ is a triplet state, we also compute the frequency for the lowest singlet state, which is found to be 4036 cm^{-1}. Going to the CCSD level, we find 3762 cm^{-1} for $[Co(EtOH)]^+$, 3763 cm^{-1} for $[Ni(EtOH)]^+$, and 3784 cm^{-1} for the bare EtOH. These results not only explain the various trends for the frequencies at the heterotetranuclear cluster, but also nicely depict the improvement of the absolute values when high-level correlations are included in the calculations.

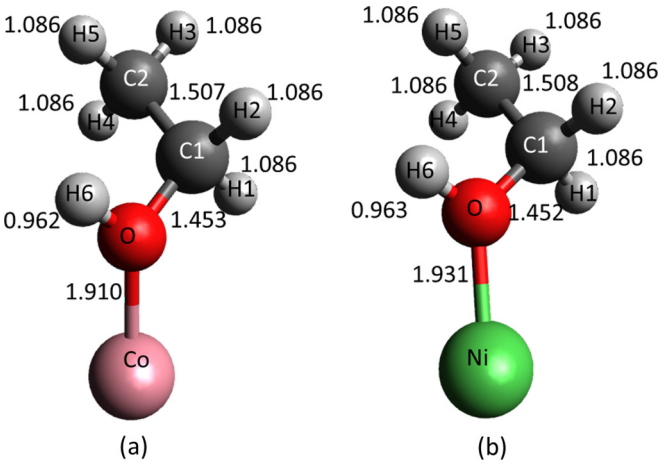

FIG. 6. Optimized $[Co(EtOH)]^+$ (a) and $[Ni(EtOH)]^+$ (b) structures, used to study the frequency shift of the OH stretching mode solely as a function of the metallic atom to which EtOH attaches (see also text). All numbers indicate bond distances in Å (the numbers next to the H atoms indicate the distance to their nearest neighbor).

IV. ULTRAFAST SPIN DYNAMICS

For our suggested ultrafast spin-dynamics scenario, we use our EOM-CCSD calculations on isomer I, since it is probably the most abundant one in the experiment (see discussion above). More specifically for SOC and spin dynamics, because for every spin quantum number s we must compute *all* substates $m_s = -s, -s+1, \ldots, s-1, s$ of a given spin multiplicity $M = 2s+1$, we need to start from pure spin states and apply single and double excitation operators in a consistent way (for details on constructing spin-adapted wave functions see, e.g., Refs. [43,48–50]). Therefore, we start from a closed-shell-based EOM-CCSD calculation (last column of Table I) and search for singlet, triplet,

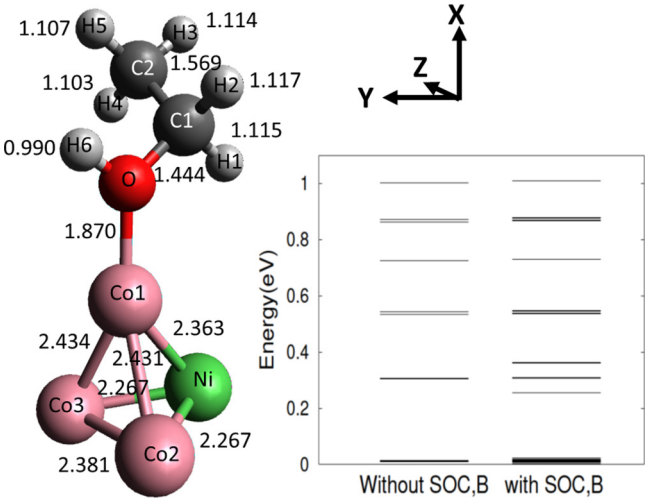

FIG. 7. Optimized structure and energy levels of the triplet states of the pyramidal isomer I with and without SOC (no singlet or quintet states are found in this energy window). All numbers indicate bond distances in Å (the numbers next to the H atoms indicate the distance to their nearest neighbor).

TABLE IV. Energies, charge, and spin densities, as well as spin directions of the initial and final states for all three local spin-flip scenarios (cf. Fig. 8). Since the states $|7\rangle$–$|9\rangle$, $|17\rangle$–$|18\rangle$, $|28\rangle$–$|30\rangle$, and $|31\rangle$–$|33\rangle$ are substates of the same triplets, they have the same charge and spin densities.

State	Energy	Charge density				Spin density				Spin ang. mom.			Orb. ang. mom.		
	(meV)	Co1	Co2	Co3	Ni	Co1	Co2	Co3	Ni	$\langle S_x\rangle$	$\langle S_y\rangle$	$\langle S_z\rangle$	$\langle L_x\rangle$	$\langle L_y\rangle$	$\langle L_z\rangle$
$\|7\rangle$	14.82	0.131	0382	0.394	−0.308	0.396	0.742	0.677	0.154	−0.039	−0.127	−0.057	−0.007	0.006	0.015
$\|9\rangle$	18.79	0.131	0382	0.394	−0.308	0.396	0.742	0.677	0.154	−0.053	0.045	0.057	−0.020	−0.020	−0.015
$\|17\rangle$	361.57	0.908	0.092	0.099	−0.462	1.028	0.277	0.263	0.398	−0.365	0.040	0.008	−0.592	0.056	0.000
$\|18\rangle$	363.98	0.908	0.092	0.099	−0.462	1.028	0.277	0.263	0.398	0.366	−0.029	0.006	0.592	−0.056	−0.001
$\|28\rangle$	867.93	−0.010	0.217	0.666	−0.276	0.210	0.454	1.103	0.209	−0.202	−0.427	−0.285	−0.005	−0.012	−0.017
$\|29\rangle$	869.18	−0.010	0.217	0.666	−0.276	0.210	0.454	1.103	0.209	−0.244	0.444	−0.367	−0.028	0.054	0.049
$\|30\rangle$	869.86	−0.010	0.217	0.666	−0.276	0.210	0.454	1.103	0.209	0.441	−0.023	0.648	0.035	−0.044	0.069
$\|31\rangle$	876.81	−0.044	0.712	0.222	−0.277	0.216	1.102	0.442	0.217	−0.542	−0.551	−0.440	−0.012	−0.024	−0.022
$\|32\rangle$	877.36	−0.044	0.712	0.222	−0.277	0.216	1.102	0.442	0.217	0.209	0.207	−0.363	0.009	−0.002	−0.014
$\|33\rangle$	878.00	−0.044	0.712	0.222	−0.277	0.216	1.102	0.442	0.217	0.336	0.349	0.806	0.001	0.028	0.036

and quintet states. It turns out that in the energetic window up to 1 eV only triplet states are found (Fig. 7). Subsequently, we introduce a static magnetic field $\mathbf{B}$ of magnitude $|\mathbf{B}| = 10^{-5}$ at. un. and the perturbative inclusion of spin-orbit coupling (SOC). The perturbation Hamiltonian reads

$$\hat{H}' = \sum_{i=1}^{N_{\rm el}} \frac{Z_a^{\rm eff}}{2c^2 R_i^3} \hat{\mathbf{L}} \cdot \hat{\mathbf{S}} + \sum_{i=1}^{N_{\rm el}} \mu_S \hat{\mathbf{S}} \cdot \mathbf{B} + \sum_{i=1}^{N_{\rm el}} \mu_L \hat{\mathbf{L}} \cdot \mathbf{B}. \quad (1)$$

Here $Z_a^{\rm eff}$ is the effective nuclear charge of atom a and accounts for the two-electron integral contributions to the SOC [51], $N_{\rm el}$ is the total number of electrons in the system, R_i is the position of the i-th electron, c is the speed of light in vacuum, μ_L and μ_S are the corresponding gyromagnetic ratios of orbital $\hat{\mathbf{L}}$ and spin $\hat{\mathbf{S}}$ angular momentum. The magnetic field, by lifting the degeneracy between spin-up and spin-down states (Zeeman splitting), allows us to find suitable initial and final states for laser-induced spin-flip scenarios. The SOC delivers the necessary intermediate spin-mixed states for our suggested laser-induced Λ scenarios [52,53].

Strictly mathematically speaking, $\mathbf{L}$ is not a good quantum number for nonspherical systems (for linear molecules only L_z is still a good quantum number). For larger systems, one must define a point of origin for $\hat{\mathbf{L}}$ [54]. Obviously, after SOC, $\hat{\mathbf{L}}$ and $\hat{\mathbf{S}}$ are coupled and thus the question of the point of origin becomes relevant for $\hat{\mathbf{S}}$ as well. Since in our quantum chemical calculations we use linear combinations of atomic orbitals, we follow the common practice here; namely, we consider for every atomic orbital the pertinent nucleus position as the origin. The reasoning behind this is that the localized electronic excitations to a great extent dictate the optical selection rules.

Due to the presence of the ligand, the three Co atoms become symmetrically nonequivalent, which results in a very pronounced localization of the spin density on a single metallic atom. Without EtOH, inspection of the spin density (not presented here) reveals that the spin is localized either on the Ni atom or equidistributed among *all* three Co atoms (Table IV).

The propagation in time of the wave functions is done in the Hilbert space spanned by the eigenvectors of $\hat{H}_0 + \hat{H}'$ (where $\hat{H}_0$ is the system's unperturbed Hamiltonian), within the semiclassical approximation, in which our system is treated fully quantum mechanically and the electric field of the laser pulse classically. This is perfectly fine for laser pulses, weak enough not to destroy the system, and strong enough so that no photon counting is necessary. The time propagation is performed under the electric dipole approximation in the interaction picture, and no relaxation is taken into account (in this time regime one can safely assume that no decoherence due to electron-phonon interaction sets in [35,55]). The time-dependent Hamiltonian reads

$$\hat{H}_{\rm laser}(t) = \hat{\mathbf{D}} \cdot \mathbf{E}_{\rm laser}(t), \quad (2)$$

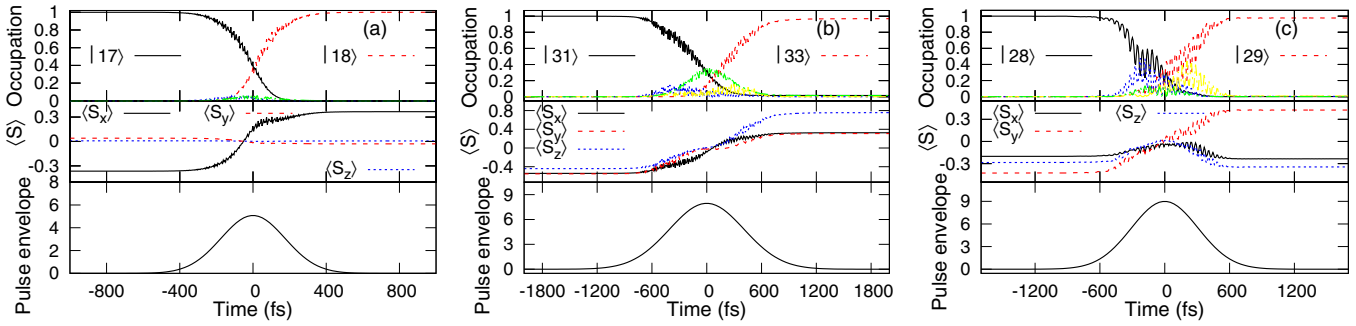

FIG. 8. Spin-flip process on (a) Co1, (b) Co2, and (c) Co3. For each process the top panel presents the time-resolved populations of the initial (dashed), final (solid), and intermediate (dotted) states, the middle panel shows the time-resolved expectation values of the $\langle \hat{S}_x \rangle$, $\langle \hat{S}_y \rangle$, and $\langle \hat{S}_z \rangle$ operators, and the bottom panel is the laser pulse envelope (in 10^{-3} at. un.).

TABLE V. Parameters of the optimized laser pulses for the three local spin-flip processes. θ and ϕ denote the angles of incidence in spherical coordinates, respectively, and γ is the angle between the polarization plane and the optical plane. FWHM is the full width half maximum of the laser pulse envelope. The arrows indicate the direction of spins. The time-dependent populations are shown Fig. 8.

Localization	Scenario	Fidelity	Parameters of the laser pulses					
			θ (°)	ϕ (°)	γ (°)	Intensity (J s^{-1}m^{-2})	FWHM (fs)	Energy (eV)
Co1	$\|\leftarrow\rangle \Longrightarrow \|\rightarrow\rangle$	0.999	− 149.0	130.9	− 157.7	0.006	411	0.277
Co2	$\|\swarrow\rangle \Longrightarrow \|\nearrow\rangle$	0.968	169.2	348.4	29.9	0.015	961	1.015
Co3	$\|\downarrow\rangle \Longrightarrow \|\uparrow\rangle$	0.977	95.3	− 22.0	187.1	0.018	728	0.470

where $\mathbf{E}_{\text{laser}}(t)$ is the time-dependent electric field, and $\hat{\mathbf{D}}$ is the electric-dipole operator. The system, being open, exchanges angular momentum with the laser pulse: The electric field of the laser couples to the orbital angular momentum, which, in turn, couples to the spins through SOC. Thus the laser serves as an angular momentum reservoir [53]. Including higher-order transitions (i.e., magnetic-dipole and electric-dipole transitions) only slightly shifts the resonance conditions, without altering the overall nature of the Λ processes. Especially the magnetic-dipole transitions would also allow for a direct spin flip (going from a spin down directly to a spin-down state) but this path is orders of magnitude slower than the Λ processes [56]. For all our suggested scenarios, we find the optimized laser parameters (i.e., direction of incidence, intensity, and duration) with a specially developed genetic algorithm [7].

Thanks to the symmetry-breaking EtOH, for the energetically low electronic states, we always find the spin density to be mainly localized on one of the Co atoms, which allows us to derive three different local spin-switching scenarios (one for each Co atom). Figure 8 depicts the time evolution of the electronic states for the three scenarios, while Table V summarizes the respective laser parameters. All scenarios are reversible; however, the best fidelity of the opposite spin-flip direction is achieved with different laser pulses.

It is interesting that, although all three spin-flip scenarios are similar, there are still some differences. The flip on Co1 is about 25% faster than the other two, which can be attributed to the fact that it has the lowest local symmetry (since the EtOH is attached to it). This asymmetry renders the optical transition matrix elements somewhat stronger (we remind the reader that in the perfect spherical symmetry of an isolated atom, the $d \leftrightarrow d$ transitions are forbidden), and therefore the electronic transitions are faster. Furthermore, since only two intermediate states are needed (states $|7\rangle$ and $|9\rangle$ with energies 0.01482 and 0.01879 eV, respectively), the resonance condition is better fulfilled, thus yielding a 99.9% fidelity, while the spin flips on Co2 and Co3 are somewhat less perfect. Those latter scenarios necessitate three intermediate states each. For the Co2 spin-flip these are states $|28\rangle$, $|30\rangle$, and $|32\rangle$ with energies 0.86793, 0.86986, and 0.87736 eV, respectively, while for the Co3 spin flip, these are states $|31\rangle$, $|32\rangle$ and $|33\rangle$ with energies 0.87681, 0.87736, and 0.87800 eV, respectively. Note also that for those two spin flips, the intermediate states are *not* Λ states, in the sense that their energy difference from the respective initial and final states are not resonant to the laser frequency. In fact, here we are dealing with a flipping spin-bounce M process [50], in which all populated states are energetically very near and the spin density of the transient state is localized on a *different* atom than the one on which the spin flip scenario takes place (Fig. 9). The interplay of the two spin localizations is also evident in the MO composition of states $|28\rangle$–$|30\rangle$ (localized on Co3) and $|31\rangle$–$|33\rangle$ (localized on Co2). For the former ones the main virtual excitations are MO(47)→ MO(71) with amplitude 0.26 and MO(49)→ MO(77) with amplitude 0.30. For the latter ones, the main virtual excitations are MO(47)→ MO(77) with amplitude 0.27 and MO(49)→ MO(71) with amplitude 0.29.

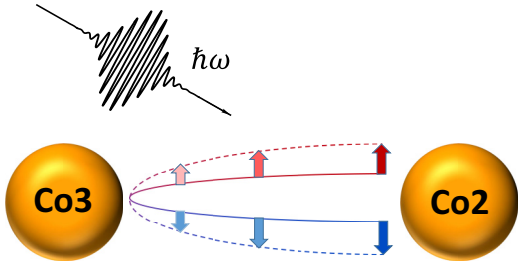

FIG. 9. Schematic of the flipping spin bounce process. Through an M process the spin get transiently transferred from Co2 to Co2 and back, while at the same time it flips its orientation.

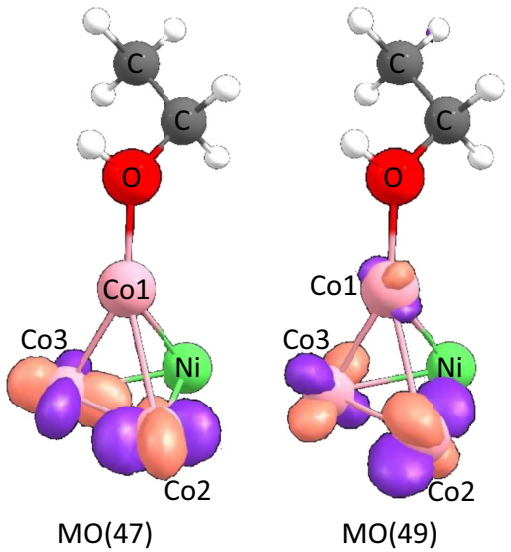

FIG. 10. Molecular orbitals MO(47) and MO(49) of isomer I, which participate in the main virtual excitation of many-electron states $|28\rangle$ to $|33\rangle$. These comprise the initial, final, and main intermediate states for the laser-induced, flipping spin bounce M processes, which locally flip the spins on Co2 and Co3 (see text and cf. Fig. 9).

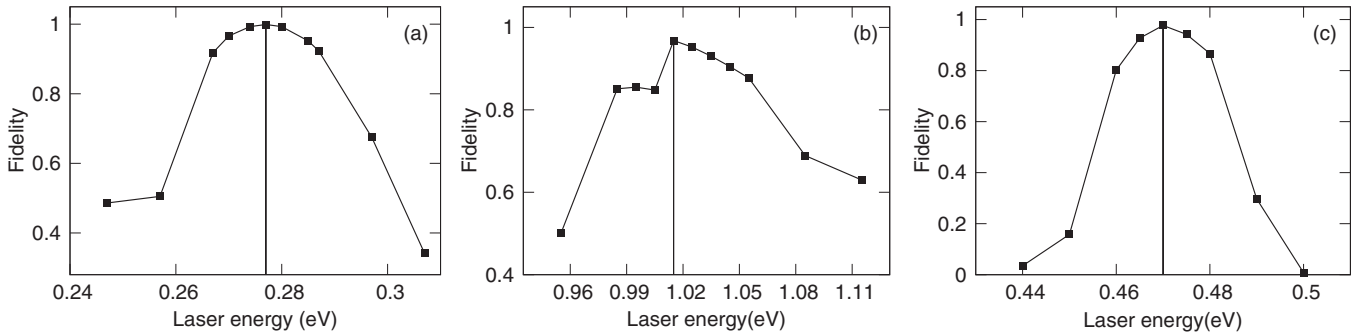

FIG. 11. Fidelity of the laser-induced spin-flip processes as functions of the laser frequency for the cases of (a) Co1, (b) Co2, and (c) Co3. The vertical lines indicate the respective optimized laser pulses (see also Table V). Only the energies are varied, all other parameters are kept to their optimized values.

In Fig. 10, one clearly sees the admixture of *d* orbitals from Co2 and Co3 (the contribution from Co1 is much smaller).

This magnetic cooperative effect very much resembles the one found previously on the homodinuclear $[Ni^{II}_2(\mathbf{L}\text{-}\mathbf{N}_4Me_2)(emb)]$ cluster, in which the spin flip was taking place on the octahedral Ni atom, while the intermediate state had a charge transfer state stemming from the square planar Ni [34].

As a final consideration toward the experimental applicability of our suggested spin-flip scenarios, we investigate the tolerance of all three scenarios with respect to the laser frequency and find that even for a detuning of the order of 20 meV in all three cases, a significant portion of the spin density gets flipped (Fig. 11).

V. CONCLUSIONS

In summary, we presented a joint experimental and theoretical study of heterotetranuclear $[Co_3Ni(EtOH)]^+$ cluster, which is formed in a laser ablation source in a molecular beam experiment. Our main findings are: (i) By comparing the experimental IR frequency of the OH stretching mode (ν_{OH}) with the theoretical calculations, we assign two different metal core geometries. One planar rhombic core with a dissociated EtOH and a pyramidal core with an intact EtOH attached. The latter geometry with the ethanol bound to cobalt is chosen for further theoretical investigations. (ii) By analyzing the theoretically optimized geometries and the trends of the different theoretical calculations regarding the frequency shifting of ν_{OH}, we find that the results get improved qualitatively by adding correlations to our calculations, and by accurately taking into account the complete normal mode of the cluster. Further quantitative improvement results from considering anharmonicities in the normal modes. (iii) Due to the symmetry-lowering effect of the attached EtOH, we can find electronic states for which the spin density is localized on one of the three Co atoms and with the use of a genetic algorithm we suggest ultrafast laser-induced spin-flip processes for each Co atom. (iv) For the case of the spin-flip on the Co2 atom, we actually identify this as an M process, resulting from a cooperative effect. It is a spin-flipping bounce process, in which the spin density gets transiently transferred from Co2 to Co3 before it returns to Co2 but this time pointing in the opposite direction. Our findings represent an additional step toward the realization of real-life, ultrafast, laser-controlled nanospintronics applications.

ACKNOWLEDGMENTS

The authors would like to acknowledge funding from the German Research Foundation (Deutsche Forschungsgemeinschaft, DFG) through the Collaborative Research Center SFB/TRR 88 “3MET” (Subprojects A2 and C2).

[1] E. Beaurepaire, J.-C. Merle, A. Daunois, and J.-Y. Bigot, Phys. Rev. Lett. **76**, 4250 (1996).
[2] J.-W. Kim, M. Vomir, and J.-Y. Bigot, Phys. Rev. Lett. **109**, 166601 (2012).
[3] F. D. Longa, J. T. Kohlhepp, W. J. M. de Jonge, and B. Koopmans, Phys. Rev. B **75**, 224431 (2007).
[4] A. Langenberg, K. Hirsch, A. Ławicki, V. Zamudio-Bayer, M. Niemeyer, P. Chmiela, B. Langbehn, A. Terasaki, B. v. Issendorff, and J. T. Lau, Phys. Rev. B **90**, 184420 (2014).
[5] C. Jamorski, A. Martinez, M. Castro, and D. R. Salahub, Phys. Rev. B **55**, 10905 (1997).
[6] G. P. Zhang, Phys. Rev. Lett. **101**, 187203 (2008).
[7] T. Hartenstein, C. Li, G. Lefkidis, and W. Hübner, J. Phys. D: Appl. Phys. **41**, 164006 (2008).
[8] V. E. Bondybey, J. Chem. Phys. **74**, 6978 (1981).
[9] T. G. Dietz, M. A. Duncan, D. E. Powers, and R. E. Smalley, J. Chem. Phys. **74**, 6511 (1981).
[10] N. C. Polfer, Chem. Soc. Rev. **40**, 2211 (2011).
[11] J. Roithová, Chem. Soc. Rev. **41**, 547 (2012).
[12] H. Yoshida, A. Terasaki, K. Kobayashi, M. Tsukada, and T. Kondow, J. Chem. Phys. **102**, 5960 (1995).
[13] N. R. Walker, R. S. Walters, E. D. Pillai, and M. A. Duncan, J. Chem. Phys. **119**, 10471 (2003).
[14] A. D. Boese, H. Schneider, A. N. Gloss, and J. M. Weber, J. Chem. Phys. **122**, 154301 (2005).
[15] A. N. Gloess, H. Schneider, J. M. Weber, and M. M. Kappes, J. Chem. Phys. **128**, 114312 (2008).

[16] S. Hirabayashi, R. Okawa, M. Ichihashi, Y. Kawazoe, and T. Kondow, J. Chem. Phys. **130**, 164304 (2009).

[17] P. M. Bialach, M. Braun, A. Lüchow, and M. Gerhards, Phys. Chem. Chem. Phys. **11**, 10403 (2009).

[18] P. M. Bialach, A. Funk, M. Weiler, and M. Gerhards, J. Chem. Phys. **133**, 194304 (2010).

[19] M. A. Duncan, Rev. Sci. Instrum. **83**, 41101 (2012).

[20] W. Jin, M. Becherer, D. Bellaire, G. Lefkidis, M. Gerhards, and W. Hübner, Phys. Rev. B **89**, 144409 (2014).

[21] B. J. Knurr and J. M. Weber, J. Phys. Chem. **118**, 4056 (2014).

[22] L. Chen, Q. Zhu, and R. Wu, Int. J. Hydrogen **36**, 2128 (2011).

[23] I. Swart, F. M. F. de Groot, B. M. Weckhuysen, P. Gruene, G. Meijer, and A. Fielicke, J. Phys. Chem. A **112**, 1139 (2008).

[24] D. M. Kiawi, J. M. Bakker, J. Oomens, W. J. Buma, Z. Jamshidi, L. Visscher, and L. B. F. M. Waters, J. Phys. Chem. A **119**, 10828 (2015).

[25] N. Kirchner, J. van Slageren, B. Tsukerblat, O. Waldmann, and M. Dressel, Phys. Rev. B **78**, 094426 (2008).

[26] W. Hübner, Y. Pavlyukh, G. Lefkidis, and J. Berakdar, Phys. Rev. B **96**, 184432 (2017).

[27] D. Chaudhuri, G. Lefkidis, and W. Hübner, Phys. Rev. B **96**, 184413 (2017).

[28] C. J. Gómez-García, E. Coronado, J. J. Borrás-Almenar, M. Aebersod, H. U. Güdel, and H. Mutka, Physica B (Amsterdam) **180-181**, 238 (1992).

[29] S. Sagar, S. Saravanan, S. Suresh Kumar, S. Venkatachalam, and M. R. Anantharaman, J. Phys. D **39**, 1678 (2006).

[30] J. Merino, A. C. Jacko, A. L. Khosla, and B. J. Powell, Phys. Rev. B **96**, 205118 (2017).

[31] A. R. Rocha, V. García-suárez, S. W. Bailey, C. J. Lambert, J. Ferrer, and S. Sanvito, Nat. Mater. **4**, 335 (2005).

[32] C. Li, T. Hartenstein, G. Lefkidis, and W. Hübner, Phys. Rev. B **79**, 180413 (2009).

[33] C. Li, W. Jin, H. Xiang, G. Lefkidis, and W. Hübner, Phys. Rev. B **84**, 054415 (2011).

[34] W. Jin, F. Rupp, K. Chevalier, M. M. N. Wolf, M. C. Rojas, G. Lefkidis, H.-J. Krüger, R. Diller, and W. Hübner, Phys. Rev. Lett. **109**, 267209 (2012).

[35] H. Xiang, G. Lefkidis, and W. Hübner, Phys. Rev. B **86**, 134402 (2012).

[36] C. Li, J. Liu, S. Zhang, G. Lefkidis, and W. Hübner, Carbon **87**, 153 (2015).

[37] V. A. Rassolov, J. A. Pople, M. A. Ratner, and T. L. Windus, J. Chem. Phys. **109**, 1223 (1998).

[38] T. Koga, H. Tatewaki, H. Matsuyama, and Y. Satoh, Theor. Chem. Acc. **102**, 105 (1999).

[39] R. E. Easton, D. J. Giesen, A. Welch, C. J. Cramer, and D. G. Truhlar, Theor. Chem. Acc. **93**, 281 (1996).

[40] J. S. Binkley, J. A. Pople, and W. J. Hehre, J. Am. Chem. Soc. **102**, 939 (1980).

[41] W. J. Hehre, R. F. Stewart, and J. A. Pople, J. Chem. Phys. **51**, 2657 (1969).

[42] N. Godbout, D. R. Salahub, J. Andzelm, and E. Wimmer, Can. J. Chem. **70**, 560 (1992).

[43] A. Szabo and N. S. Ostlund, *Modern Quantum Chemistry* (Dover Publications, Inc., New York, 1996).

[44] D. R. Yarkony, *Modern Electronic Structure Theory: Part I* (World Scientific Publishing Co. Pte. Ltd., Singapore, 1995).

[45] M. W. Schmidt, K. K. Baldridge, J. A. Boatz, S. T. Elbert, M. S. Gordon, J. H. Jensen, S. Koseki, N. Matsunaga, K. A. Nguyen, S. Su, T. L. Windus, M. Dupuis, and J. A. Montgomery, J. Comput. Chem. **14**, 1347 (1993).

[46] M. J. Frisch, G. W. Trucks, H. B. Schlegel, G. E. Scuseria, M. A. Robb, J. R. Cheeseman, J. A. Montgomery, Jr., T. Vreven, K. N. Kudin, J. C. Burant, J. M. Millam, S. S. Iyengar, J. Tomasi, V. Barone, B. Mennucci, M. Cossi, G. Scalmani, N. Rega, G. A. Petersson, H. Nakatsuji, M. Hada, M. Ehara, K. Toyota, R. Fukuda, J. Hasegawa, M. Ishida, T. Nakajima, Y. Honda, O. Kitao, H. Nakai, M. Klene, X. Li, J. E. Knox, H. P. Hratchian, J. B. Cross, V. Bakken, C. Adamo, J. Jaramillo, R. Gomperts, R. E. Stratmann, O. Yazyev, A. J. Austin, R. Cammi, C. Pomelli, J. W. Ochterski, P. Y. Ayala, K. Morokuma, G. A. Voth, P. Salvador, J. J. Dannenberg, V. G. Zakrzewski, S. Dapprich, A. D. Daniels, M. C. Strain, O. Farkas, D. K. Malick, A. D. Rabuck, K. Raghavachari, J. B. Foresman, J. V. Ortiz, Q. Cui, A. G. Baboul, S. Clifford, J. Cioslowski, B. B. Stefanov, G. Liu, A. Liashenko, P. Piskorz, I. Komaromi, R. L. Martin, D. J. Fox, T. Keith, M. A. Al-Laham, C. Y. Peng, A. Nanayakkara, M. Challacombe, P. M. W. Gill, B. Johnson, W. Chen, M. W. Wong, C. Gonzalez, and J. A. Pople, *Gaussian 03, Revision C.02* (Gaussian, Inc., Wallingford, CT, 2004).

[47] M. Scheer, C. A. Brodie, R. C. Bilodeau, and H. K. Haugen, Phys. Rev. A **58**, 2051 (1998).

[48] H. Nakatsuji, SAC-CI method: Theoretical aspects and some recent topics, in *Computational Chemistry: Reviews of Current Trends*, Vol. 2 (World Scientific, Singapore, 1997), Chap. 2.

[49] R. Pauncz, *Spin Eigenfunctions: Construction and Use* (Springer, New York, 1979).

[50] D. Chaudhuri, H. P. Xiang, G. Lefkidis, and W. Hübner, Phys. Rev. B **90**, 245113 (2014).

[51] S. Koseki, M. W. Schmidt, and M. S. Gordon, J. Phys. Chem. A **102**, 10430 (1998).

[52] G. Lefkidis and W. Hübner, Phys. Rev. B **87**, 014404 (2013).

[53] G. Lefkidis, G. P. Zhang, and W. Hübner, Phys. Rev. Lett. **103**, 217401 (2009).

[54] B. R. Judd, *Angular Momentum Theory for Diatomic Molecules* (Academic Press, Inc., New York, 1975).

[55] J.-Y. Bigot, M. Vomir, and E. Beaurepaire, Nat. Phys. **5**, 515 (2009).

[56] R. Gómez-Abal, O. Ney, K. Satitkovitchai, and W. Hübner, Phys. Rev. Lett. **92**, 227402 (2004).